Enhanced CO resistance of Pd/SSZ-13 for passive NOx adsorption

Chemical Engineering Journal 460 (2023) 141681

Contents lists available at ScienceDirect

Chemical Engineering Journal

journal homepage: www.elsevier.com/locate/cej

Enhanced CO resistance of Pd/SSZ-13 for passive NO_x adsorption

Dawei Yao [a], Phuoc Hoang Ho [a], Rojin Feizie Ilmasani [a], Johann C. Wurzenberger [b], Thomas Glatz [b], Derek Creaser [a], Louise Olsson [a,*]

[a] Chemical Engineering Division, Competence Center for Catalysis, Chalmers University of Technology, Göteborg SE-41296, Sweden
[b] AVL List GmbH, Graz, Austria

ARTICLE INFO

Keywords:
Passive NOx adsorption
Pd sintering
CO tolerance
Ostwald ripening
Kinetic model

ABSTRACT

Passive NO_x adsorption (PNA) is a novel technology to control NO_x emissions during cold start. However, the recent generation of PNA material, Pd/zeolite, suffers from major degradation under high CO concentrations. In this work, we developed a novel form of Pd/SSZ-13 by using a freeze-drying process after incipient wetness impregnation. This Pd/SSZ-13 showed a better stability than the sample synthesized by the common process. Several characterization measurements were conducted and it was found that the Pd sites on the freeze-dried sample were more resistant towards CO-induced agglomeration. By combing in-situ characterization and kinetic modeling, we found that the freeze-dried Pd/SSZ-13 had more ion-exchanged Pd sites, which provided greater resistance towards the CO-induced Ostwald ripening process, and consequently suppressed the sintering behavior under a high CO concentration. This material offers a potentially improved stability of PNAs under extremely high CO concentration pulses from incomplete diesel combustion during engine cold start.

1. Introduction

Diesel fuel combustion in engines is considered one of the main sources of nitrogen oxides (NO_x) emissions [1,2]. With the gradual expansion of the automotive market and the tightening of emission standards, the responsibility of aftertreatment systems is becoming heavier. The current popular aftertreatment configurations are constructed by the following modules typically in this sequence: diesel oxidation (DOC) catalysts, diesel particulate filter (DPF), selective catalytic reduction (SCR) unit and ammonia slip catalyst (ASC) [3]. Owing to the new regulations on cold start of engines and the very low emission temperature it is critical that the NO_x emissions are limited [4]. Under cold start conditions, urea decomposition and the SCR rate are significantly suppressed, resulting in an insufficient NO_x control of current aftertreatment configurations [5,6]. To solve this problem, a new technology named passive NO_x adsorbers (PNA) was created to adsorb NO_x species at low temperatures, and thermally release NO_x when the engine warms up [6,7]. The released NO_x is further converted in the SCR module, enabling efficient control of the NO_x emissions.

The PNA module is usually designed to be placed in front of the other aftertreatment modules to adsorb NO_x species during cold start. Therefore, the PNA usually works under harsh conditions, including high concentrations of H_2O, SO_2, CO, hydrocarbons, etc. [8,9]. Furthermore, owing to the incomplete combustion of diesel during cold start, CO pulses with extremely high concentrations are generated that can account for 80 % of CO release under the duration of a total driving cycle [10]. In the current generation of PNA, Pd/zeolite is usually chosen owing to its high resistance towards SO_2 and H_2O [2,6]. It also offers excellent performance for oxidation of CO and HC [1,11] which can potentially replace the DOC module. Although the performance of Pd/zeolite is fascinating as PNA, it still has degradation issues induced by high concentrations of CO [12–14]. Several works have demonstrated that Pd sites suffer from irreversible agglomeration under high CO concentration exposure [8,15,16]. In our recent work, we found there are two sintering modes of Pd sites during degradation of the PNA [17]: 1) Under high CO concentration, Pd sites tend to adsorb CO and form Pd carbonyl, which has high mobility at low temperature [18]. When the engine warms up, Pd carbonyls start to agglomerate and release CO to form Pd nanoparticles (NPs). This process is called Ostwald ripening [19,20]. 2) The generated Pd NPs are unstable at high working temperature of the engine and thus migrate to form larger Pd NPs, which is called a particle migration process [19,21].

Therefore, improving the stability of a PNA under high CO concentration has become a major challenge in developing PNA modules. In this work, we chose Pd/SSZ-13, which presents considerable NO_x storage performance [9,22], as the model material for a PNA. We adjusted

* Corresponding author.
E-mail address: louise.olsson@chalmers.se (L. Olsson).

https://doi.org/10.1016/j.cej.2023.141681
Received 16 November 2022; Received in revised form 19 January 2023; Accepted 31 January 2023
Available online 2 February 2023

the distribution of different Pd sites by simply modifying the drying conditions after incipient wetness impregnation, and further conducted multicycle PNA evaluation in the presence of NO_x, O_2, H_2O, and high CO concentration. We found that the freeze-dried PNA sample showed a better stability than the sample dried at 80 °C (a common drying process). Especially, in the first cycle under an extremely high CO concentration (~4000 ppm), the 80 °C-dried PNA sample suffered significant degradation while the freeze-dried PNA still maintained the same NO_x storage amount. To the best of our knowledge, this is the first study where it is shown that the PNA degradation could be suppressed by adding a freeze-drying step. Several characterizations were used to investigate the changes in the different Pd of Pd/SSZ-13 before and after the tests. We found the PdO_x sites on the external surface of SSZ-13 and ion-exchanged Pd sites in SSZ-13, presented different resistance towards high CO concentration by their susceptibility to the Ostwald ripening process. A kinetic model was further applied to investigate the sintering mode of different Pd sites, and simulated the PNA performance after ceasing CO exposure.

2. Experimental methods

2.1. PNA preparation

2.1.1. Pd/SSZ-13 preparation

Na-SSZ-13 with a Si/Al = 12 was synthesized according to the same method as in our previous studies [17,23]. Briefly, 1.6 g NaOH, 35.16 g TMAda-OH, 2.76 g $Al(OH)_3$ and 24 g SiO_2 were mixed into 132 mL deionized water with vigorous stirring until the mixture became a gel. The mixture was transferred into an autoclave, then placed into an oven and heated up to 160 °C for 96 h under rotation stirring. After cooling to room temperature, the mixture was separated via centrifugation and washed with 900 mL of deionized water. The obtained sample was dried at 80 °C for 6 h and calcinated at 600 °C for 8 h.

NH_4-SSZ-13 was obtained via an ion-exchange process. 15 g Na-SSZ-13 was mixed into 300 mL NH_4NO_3 solution (1 mol/L) and heated up to 80 °C, then washed by 800 mL deionized water. This ion-exchange process was repeated twice to ensure that the Na ion was completely removed. The obtained sample was dried at 80 °C for 6 h.

Pd/SSZ-13 samples were obtained via an incipient wetness impregnation method. 1 wt% Pd was loaded via impregnation of a $Pd(NO_3)_2$ solution on NH_4-SSZ-13. After that, the sample was dried via different processes. In one process the sample was dried by freeze drying. Briefly, the sample was put into a vacuum beaker, then placed into liquid nitrogen to ensure the sample was frozen. Then the beaker was placed under a vacuum to 5 hPa and kept for 24 h to sublimate H_2O. After drying the sample was calcined at 500 °C for 5 h. The obtained sample will be referred to as 'Fredry'. Another sample after impregnation was dried at 80 °C overnight and calcined at 500 °C for 5 h, which is a common method to load Pd on SSZ-13 [22,24,25]. This sample will be referred to as '80dry'.

2.1.2. Monolith preparation

The cordierite monoliths were shaped as a honeycomb structure with a cpsi of 400. The monoliths were cut into small cylinders (2 cm length × 2.1 cm diameter), then calcinated at 550 °C for 2 h to clean the channel surface. 5 wt% Pd/SSZ-13 samples were mixed with 95 wt% Boehmite (Dispersal *P*2) and dispersed into a 1:1 ethanol/H_2O solution. The mixture was dropped into all the channels of the monolith and dried at 80 °C. This loading procedure was repeated several times until the weight of the washcoat reached 700 ± 7 mg. A calcination process at 500 °C for 5 h was then conducted for the loaded monolith.

2.2. Reactor system

The PNA evaluation system has been described in our previous work [26–31], which contains several mass flow controllers, a H_2O evaporation system, a reactor tube with two thermocouples, and an FTIR spectrometer (MKS Multigas 2030) to detect the outlet gases. The monolith was placed inside the reactor tube and two thermocouples were separately placed in the upstream of the monolith and inside the monolith channel.

2.2.1. Degreening of the monoliths

A degreening process was firstly conducted on all samples before the PNA evaluation and material characterization to generate more Pd sites from the ion-exchange stage and to stabilize the PNA sample [32]. The monolith was loaded into the reactor, and treated at 750 °C under 400 ppm NO_x, 5 % H_2O, and 8 % O_2 with a total flow rate of 900 mL/min. After that, the monolith was kept at 750 °C in Ar to remove adsorbed species then cooled to 80 °C for the following evaluation, or cooled to room temperature and taken out for other characterizations.

2.2.2. Adsorbent evaluation

After degreening the monolith, an 8-cycle PNA evaluation process was conducted. To test the resistance of the PNA towards CO, cycles 3–7 were conducted with the addition of CO in 200 ppm NO_x, 8 % O_2 and 5 % H_2O, while cycles 1, 2, and 8 were conducted without CO. Every evaluation cycle contains three processes to resemble the engine's cold start period:

1) NO_x adsorption at low temperature: 80 °C, 200 ppm NO_x, 4000 ppm CO (added in cycles 3–7), 5 % H_2O, 8 % O_2, balance in Ar, maintained for 45 min.
2) Temperature programmed desorption (TPD): maintained the same gas conditions, increased the temperature to 550 °C with a rate of 10 °C/min, then kept for 15 min.
3) Regeneration process: for the cycles without adding CO (cycles 1, 2 and 8), NO_x was first stopped and then the system was maintained at 550 °C for 5 min, then cooled down to 80 °C for the next cycle. To accurately track the degradation behavior of different PNA samples under high concentration CO, the regeneration process is removed for the cycles with CO to prevent the redispersion of Pd sites. In these cycles, NO_x and CO feed were stopped and the system was directly cooled down to 80 °C without holding the temperature at 550 °C.

The scheme of temperature and inlet gas conditions is shown in Figure S1, Supplementary Information (SI).

2.3. Characterization

Transmission electron microscopy (TEM) was conducted by an FEI Tecnai with a voltage of 200 kV. For preparing the TEM sample, the powder was dispersed into ethanol, then dropped onto a copper grid supported carbon film. Around 100 Pd particles were measured in every sample in TEM images to obtain the statistical information regarding to diameters distribution and average diameters.

X-ray diffraction (XRD) was conducted with a Bruker D8 Discover with voltage of 40 kV and current of 40 mA. Cu Kα radiation (λ = 1.5418 Å) was used as the radiation source and filtered at room temperature. The XRD pattern was obtained by scanning from 10° to 60° with a rate of 1°/min.

In-situ diffuse reflectance infrared Fourier transform spectroscopy (DRIFTS) of CO adsorption was conducted by a Bruker Vertex 70 spectrometer equipped with several mass flow controllers, a H_2O evaporator, an in-situ diffuse chamber with two CaF windows and an MCT detector. The degreened or tested Pd/SSZ-13 samples were first scratched from the wall of the monolith, then 20 mg of them were placed into the in-situ chamber. The samples were thereafter first treated at 200 °C under pure Ar, then cooled down to 30 °C. After cooling to 30 °C the background was collected. With scanning at 30 °C with a resolution of 4 cm^{-1}, 4000 ppm CO in Ar was added for 20 min, then pure Ar was added for 5 min to purge the gas phase CO.

CO chemisorption was conducted by an ASAP 2020 Chemi Plus apparatus from Micromeritics Instruments Corporation, equipped with an extra chemisorption device. The powder was placed into a test tube and sealed into the device, followed by a pretreatment at 200 °C under vacuum to remove any contamination. After pretreatment the tube was cooled to 35 °C, then CO was added from 0.13 to 0.80 bar to collect the initial adsorption isotherm. After that, an evacuate process was conducted to remove the CO from physisorption, and the isotherm was repeated to collect the second isotherm. The difference between these two isotherms is the amount of chemisorbed CO.

3. Kinetic modeling

Kinetic modeling was performed based on our previous model that describes PNA performance and degradation under a large range of CO concentrations [17]. AVL BOOST^{TM} (which later will be transferred to CRUISE^{TM} M) embedded with an aftertreatment module and User Coding Interface are used for building the kinetic model and simulating the NO_x profiles. The parameters related to mass transfer and heat transfer are set according to the property database in AVL CRUISE^{TM} M. Detailed mass and heat balance equations and assumptions can be found in our previous PNA modeling works [17,23]. We here briefly introduce our kinetic model in Sections 3.1 and 3.2.

3.1. Reactor model

The reactor model consists of 3 elements: the inlet boundary, monolith, and outlet boundary. 20 grid points are applied along the system, where 18 grid points are set along the axial direction in the monolith channels, and 2 grid points for inlet and outlet boundaries. Both the mass transfer inside the washcoat and external gas phase mass transfer were considered in this model. The external mass transfer was described according to the film model [33]. The internal mass transfer was accounted for by a pore diffusion model with constant effective diffusivities, according to Chatterjee et al [34], and has been used in our previous works [17,27,28,35–37].

We assume that the radial heat transfer effect of the honeycomb catalytic converter is much smaller compared to the axial heat transfer, so the entire converter can be simplified to a single-channel model. The reaction heat of NO_x adsorption and desorption was neglected in this model due to the low NO_x concentration. This simplification has been used in many kinetic modeling works [27,29,35,36,38]. However, owing to the high concentration of CO (4000 ppm) used in the PNA evaluation, the reaction heat of CO oxidation was set based on the database of thermal properties from CRUISE M. We set the inlet temperature in the model in accordance with the measured upstream temperature of the monolith, and simulated the monolith temperature to compare with the experimental temperature measured inside the monolith.

3.2. Reactions, rate expressions and thermodynamic restrictions

The reaction rate constants are described in accordance with the Arrhenius equation:

$$k_j = A_j e^{\frac{-E_{A,j}}{(RT_s)}} \quad (1)$$

For reaction j, A_j and $E_{A,j}$ are respectively the pre-exponential factor (s^{-1}) and activation energy (J/mol), and k_j is the rate constant j (s^{-1}). The Temkin isotherm was used to linearly correlate the activation energy and adsorption coverage [39]:

$$E_{des} = E^0_{des}(1 - \alpha\theta) \quad (2)$$

where E^0_{des} is the desorption energy at zero coverage, α is the coverage dependence constant and θ is the fractional coverage.

In this work, we simulate the PNA performance according to our previous model [17,23], which contains 4 groups of reactions, as shown in Tables 1–4.

Table 1
Reaction mechanism of PNA: NO & NO_2 reactions on initial Pd sites.

Reactions	Reaction Steps
NO & NO_2 adsorb on Z$^-$Pd^{2+}Z$^-$:	
Reaction (1)	Z$^-$Pd^{2+}Z$^-$ + NO ⇌ Z$^-$Pd^{2+}Z$^-$–NO
Reaction (2)	Z$^-$Pd^{2+}Z$^-$ + NO_2 ⇌ Z$^-$Pd^{2+}Z$^-$–NO_2
NO adsorb on Z$^-$[PdOH]$^+$:	
Reaction 3	Z$^-$[PdOH]$^+$ + NO ⇌ Z$^-$[PdOH]$^+$–NO
Z$^-$[PdOH]$^+$ reduction and re-oxidation:	
Reaction 4	2Z$^-$[PdOH]$^+$–NO ⇌ Z$^-$Pd$^-$+Z$^-$Pd$^-$–NO + NO_2 + H_2O
Reaction 5	Z$^-$Pd$^-$ + NO ⇌ Z$^-$Pd$^-$–NO
Reaction 6	2Z$^-$Pd$^-$ + 0.5O_2 + H_2O ⇌ 2Z$^-$[PdOH]$^+$
Formation and decomposition of $Pd(NO_3)_2$:	
Reaction 7	PdO + 1.5O_2 + 2NO ⇌ $Pd(NO_3)_2$
Reaction 8	$Pd(NO_3)_2$ + NO ⇌ 3NO_2 + PdO
Gas phase NO oxidation:	
Reaction 9	2NO + O_2 ⇌ 2NO_2

Table 2
Reaction mechanism of PNA: NO & NO_2 reactions on initial Pd sites with the addition of CO.

Reactions	Reaction Steps
Reduction of absorbed NO_2:	
Reaction 10	Z$^-$Pd^{2+}Z$^-$–NO_2 + CO → Z$^-$Pd^{2+}Z$^-$–NO + CO_2
Z$^-$[PdOH]$^+$ reduction and re-oxidation (by CO):	
Reaction 11	2Z$^-$[PdOH]$^+$–NO + CO → 2Z$^-$Pd^{++}–NO + H_2O + CO_2
Reaction 12	2Z$^-$Pd^{++}–NO + H_2O + CO → 2Z$^-$H$^+$-Pd^0-NO + CO_2
Reaction 13	Z$^-$H$^+$-Pd^0 + NO ⇌ Z$^-$H$^+$-Pd^0-NO
Reaction 14	2Z$^-$H$^+$-Pd^0 + 0.5O_2 ⇌ 2Z$^-$Pd$^-$+ H_2O
PdO reduction and re-oxidation:	
Reaction 15	PdO + CO → Pd^0 + CO_2
Reaction 16	Pd^0 + 0.5O_2 → PdO
Reaction 17	Pd^0 + NO ⇌ Pd^0-NO
Gas phase CO oxidation:	
Reaction 18	2CO + O_2 → 2CO_2
Z$^-$Pd^{2+}Z$^-$ reduction and re-oxidation:	
Reaction 19	Z$^-$Pd^{2+}Z$^-$ +H_2O + CO → Z$^-$H$^+$+Z$^-$H$^+$-Pd^0 + CO_2
Reaction 20	Z$^-$H$^+$+Z$^-$H$^+$-Pd^0 + 0.5O_2 → Z$^-$Pd^{2+}Z$^-$ + H_2O
Reaction 21	Z$^-$H$^+$+Z$^-$H$^+$-Pd^0 + NO ⇌ Z$^-$H$^+$+Z$^-$H$^+$-Pd^0-NO

Table 1 shows the reactions of NO_x with the initial Pd species. There are two ion-exchanged Pd sites (Z$^-$Pd^{2+}Z$^-$, Z$^-$[PdOH]$^+$) and one PdO site (PdO) on the external surface of SSZ-13. Z$^-$Pd^{2+}Z$^-$ can adsorb both NO and NO_2 species and release them at higher temperatures (Reactions 1–2, R1-R2). Z$^-$[PdOH]$^+$ can adsorb NO and be reduced to a Z$^-$Pd$^-$ site, which has a stronger interaction towards NO (*R*3-R7). The PdO site forms $Pd(NO_3)_2$ species and subsequently decomposes when the temperature starts to rise, as shown in R7-R8. R9 accounts for NO oxidation at high temperatures, which is a global reaction step to simplify the model.

Table 2 describes the CO-contributed reduction reactions of Pd sites. All the Pd species with positive valence can be reduced by CO, including Z$^-$Pd^{2+}Z$^-$ (R19-R21), Z$^-$[PdOH]$^+$/Z$^-$Pd$^-$ (R11-R14), and PdO (R15-R17).

Table 3
Reaction mechanism of PNA: Ostwald ripening of initial Pd sites.

Reactions	Reaction Steps
Formation of Pd carbonyl:	
Reaction 22	$Z^-H^+ + Z^-H^+ - Pd^0 + 4CO \rightarrow 2Z^-H^+ + Pd(CO)_4$
Reaction 23	$Z^-H^+ - Pd^0 + 4CO \rightarrow Z^-H^+ + Pd(CO)_4$
Reaction 24	$Pd^0 + 4CO \rightarrow Pd(CO)_4$
Agglomerition of Pd carbonyl to Pd/PdO NPs:	
Reaction 25	$Pd(CO)_4 \rightleftharpoons Pd^{exposed(e)} + 4CO$
Reaction 26	$Pd(CO)_4 \rightarrow Pd^{covered} + 4CO$
NO and CO oxidation on Pd/PdO NPs	
Reaction 27	$Pd^e + NO \rightleftharpoons Pd^e\text{-}NO$
Reaction 28	$Pd^e\text{-}NO + O_2 \rightleftharpoons Pd^eO + NO_2$
Reaction 29	$Pd^e + 0.5O_2 \rightleftharpoons Pd^eO$
Reaction 30	$Pd^eO + NO \rightleftharpoons Pd^e + NO_2$
Reaction 31	$Pd^eO + CO \rightarrow Pd^e + CO_2$

Table 4
Reaction mechanism of PNA: Particle migration of Pd nanoparticles.

Reactions	Reaction Steps
Particle migration of Pd NPs to larger Pd/PdO NPs	
Reaction 32	$Pd^e \rightarrow Pd^{Large\ NPs(N)}$
NO and CO oxidation on large Pd/PdO NPs	
Reaction 33	$Pd^N + NO \rightleftharpoons Pd^N\text{-}NO$
Reaction 34	$Pd^N\text{-}NO + O_2 \rightleftharpoons Pd^NO + NO_2$
Reaction 35	$Pd^N + 0.5O_2 \rightleftharpoons Pd^NO$
Reaction 36	$Pd^NO + NO \rightleftharpoons Pd^N + NO2$
Reaction 37	$Pd^NO + CO \rightarrow Pd^N + CO_2$

The adsorbed NO_2 species can also be reduced by CO as shown in R10. R18 describes the gas-phase oxidation of CO.

Table 3 reactions are embedded in the model to describe the Ostwald ripening of Pd sites. The metallic Pd sites that are produced by the reduction of Pd^{2+} or Pd^- by CO, formed Pd carbonyl species as shown in R22-R24. The Pd carbonyl species have high mobility on the surface of SSZ-13 and tend to agglomerate to Pd/PdO nanoparticles (NPs), where only the surface Pd sites of the NPs are considered as the exposed active sites ($Pd^{exposed(e)}$). This process is described in R25-R26. The PdO NPs also contribute to NO_x adsorption, NO oxidation and CO oxidation, as described in R27-R31.

Table 4 reactions describe the particle migration of Pd NPs. Owing to the low stability of Pd NPs, they tend to agglomerate to form large Pd NPs ($Pd^{Large\ NPs(N)}$) at high temperatures, as shown in *R*32. The large Pd NPs also contribute to NO_x adsorption, NO oxidation and CO oxidation (R33-R37).

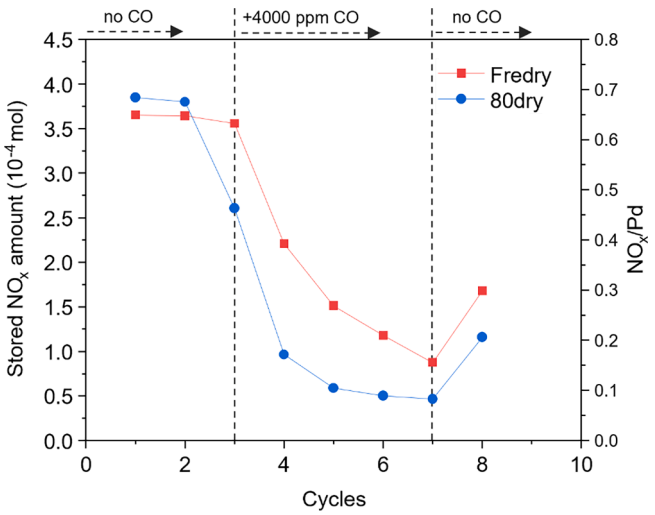

Fig. 2. Stored amount of NO_x and NO_x/Pd in each cycle.

All the detailed reaction rate expressions are shown in Table S1. Notably, owing to the different methods in synthesizing Fredry and 80dry, the PNA performances are different from our previous modeling work [17]. To fit the NO_x profiles, only the pre-exponential factors (A_i) in the Arrhenius equations and coverage dependence (α) in the Temkin isotherms are changed, while other parameters and settings are the same as in our previous model [17]. For sets of reactions that together form the overall NO oxidation reaction, the kinetic parameters of all reactions needed to follow the thermodynamic restriction, where the overall change of enthalpy and entropy respectively equal to −58 kJ/mol and −76 J/(K*mol), as listed in Table S1.

4. Result and discussion

4.1. Degradation of PNA performance under high CO concentration

Fredry and 80dry samples were first evaluated by the multicycle PNA test to obtain the degradation performance. The inlet gas conditions, temperature and outlet NO_x profiles are shown in Figure S1. There are three processes in each cycle: NO_x adsorption, TPD and regeneration, which have been described in *Section 2.2.2. Adsorbent evaluation.* The

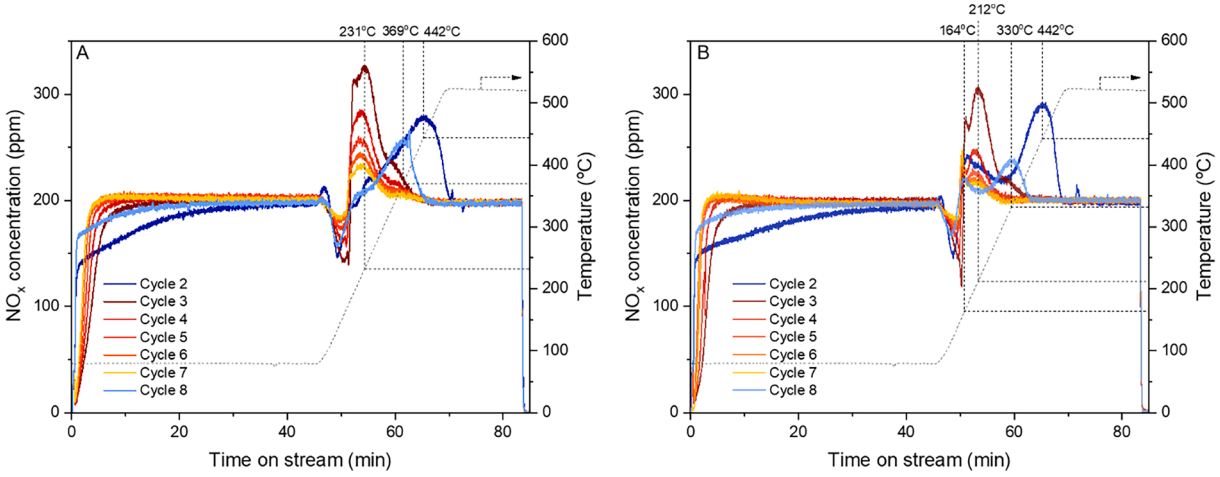

Fig. 1. A, B: NO_x profiles of each cycle in multi-cycle PNA test on Fredry (A) and 80dry (B). Inlet gas conditions: 200 ppm NO_x (196.4 ppm NO and 3.6 ppm NO_2), 4000 ppm CO (in cycles 3–7), 8 %O_2, 5 %H_2O, balanced in Ar.

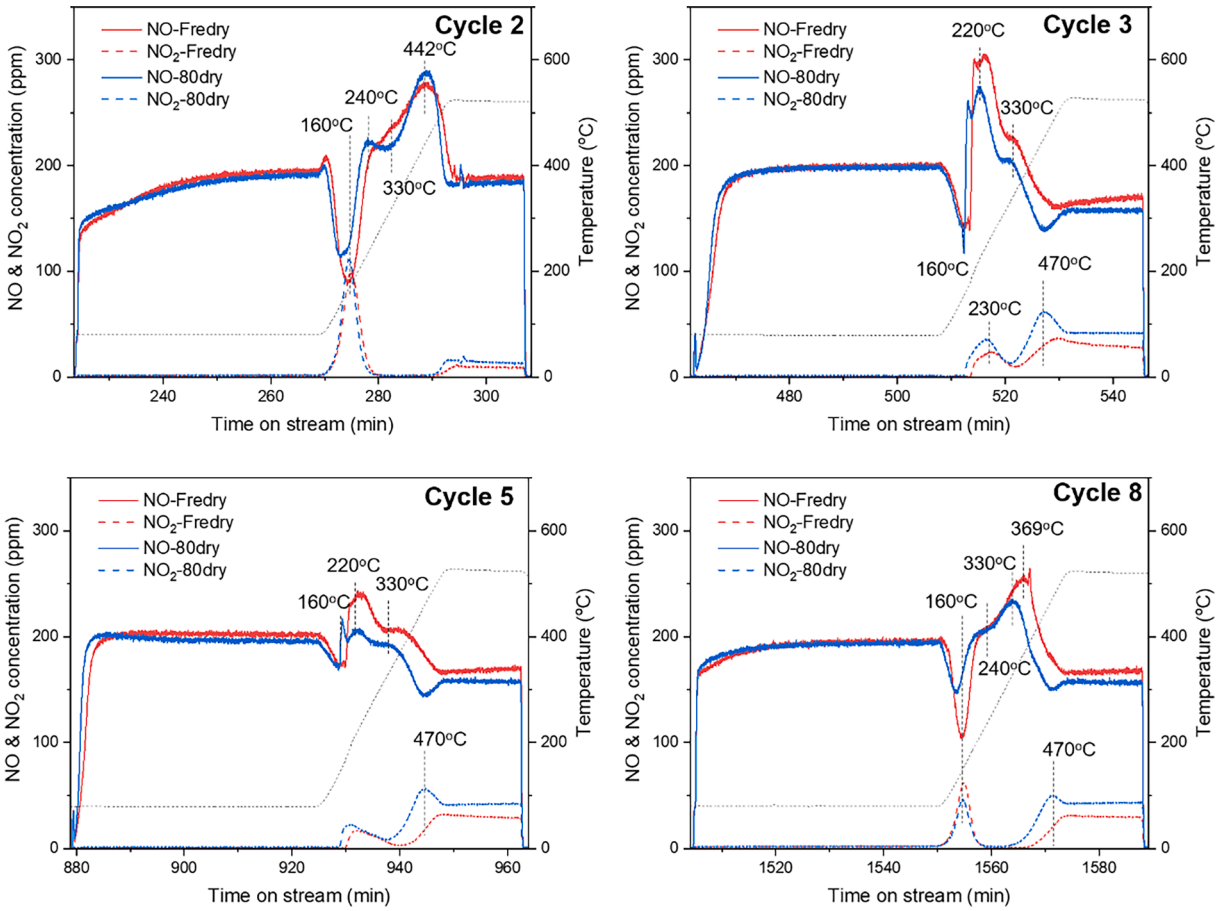

Fig. 3. NO and NO_2 profiles of selected PNA cycles. Inlet gas conditions: 200 ppm NO_x (196.4 ppm NO and 3.6 ppm NO_2), 4000 ppm CO (in cycle 3–7), 8 %O_2, 5 % H_2O, balanced in Ar. All-cycles NO/NO_2 profile is shown in Figure S3.

NO_x profiles in each cycle are shown in Fig. 1, where the time points when NO_x enters the reactor after cooling are considered as the start of each cycle. We further calculated the stored NO_x and NO_x/Pd in every cycle, as shown in Fig. 2. In the first two cycles, the test was conducted with 200 ppm NO_x but without CO to get the initial PNA performance. For both Fredry and 80dry samples, the NO_x profiles in cycle 1 and cycle 2 (Figure S2) are the same, indicating there is no degradation in the first 2 cycles. Furthermore, the NO_x adsorption amount in Fredry and 80dry is also similar.

Starting with cycle 3, 4000 ppm of CO was added during NO_x adsorption of each cycle to simulate the high concentration CO pulse during cold start. The temperature of the NO_x desorption peaks in cycle 3 was changed in both Fredry and 80dry, indicating CO inducing a change in Pd sites. Apparently, 80dry suffered a large degradation in cycle 3, while the Fredry still kept the same NO_x storage amount. With the proceeding PNA cycles, Fredry also deactivated but still showed a better NO_x storage performance than the 80dry sample. After 2 more cycles with CO, the stored NO_x amount of the 80dry reached a minimum ($\sim 0.6 \times 10^{-4}$ mol, cycle 5), while the stored NO_x amount in Fredry remained considerable, and still slowly decaying, even up to cycle 7. It was found in our previous work that the PNA sample lost 95 % NO_x storage in the first 5 cycles with the presence of 4000 ppm CO [17]. Therefore, we only tested 5 cycles with CO (cycles 3–7) in this work, and conducted cycle 8 without CO to obtain the PNA performance after CO degradation. Comparing the NO_x profiles in cycle 2 and cycle 8 in Fig. 1, it can be seen the NO_x desorption peaks shifted to lower temperatures for both Fredry and 80dry, indicating the initial Pd sites were changed. It was also shown in Fig. 2 that Fredry can adsorb more NO_x than 80dry in cycle 8, indicating the Fredry is more resistant towards the high CO concentration pulse during the multicycle cold start.

We here select NO and NO_2 profiles in 4 typical cycles (cycles 2, 3, 5, 8) to interpretate the detailed PNA performance during CO-induced degradation, as shown in Fig. 3. The NO and NO_2 profiles in all the cycles are shown in Figure S3. As reported in previous works, two Pd sites in the ion-exchange form ($Z^-Pd^{2+}Z^-$ and $Z^-[PdOH]^+$) and one external PdO site are the initial Pd sites in Pd/SSZ-13 [23]. The high concentration of CO can induce Pd carbonyl formation for all the Pd sites and leads to Ostwald ripening to form Pd nanoparticles, resulting in agglomeration and loss of the amount of accessible surface Pd sites [17]. The formed Pd nanoparticles are unstable at high working temperatures of the engine, and thus subsequently migrate into larger Pd nanoparticles [17,19]. In cycle 2 we could see that there are two NO release peaks and one NO consumption peak (to generate NO_2) for the 80dry sample. The consumption peak of NO and NO_2 generation peak at ~ 160 °C which can be attributed to the reduction of $Z^-[PdOH]^+$ to Z^-Pd^-, and the formation of Pd nitrates from PdO clusters [1,23]. The peaks at 240 °C and 442 °C can be respectively attributed to NO release from $Z^-Pd^{2+}Z^-$ and Z^-Pd^- [23,40]. In cycle 2 of Fredry we could also see the NO consumption peak and release peaks, however, the release temperature of $Z^-Pd^{2+}Z^-$–NO (330 °C) is higher than that of 80dry (240 °C), indicating the $Z^-Pd^{2+}Z^-$ in Fredry shows stronger interaction towards NO.

After adding CO, both Fredry and 80dry are gradually deactivated, and present different NO and NO_2 profiles compared to the initial cycles, as shown in Fig. 3. Cycle 3 is the first cycle tested with 4000 ppm CO, causing the NO release temperature to become lower for both Fredry and 80dry samples. This is because the ion-exchanged Pd sites were reduced to metallic Pd species (Pd clusters or Z^-H^+-Pd^0), which have weaker interaction with NO. The NO release peak positions for Fredry and 80dry

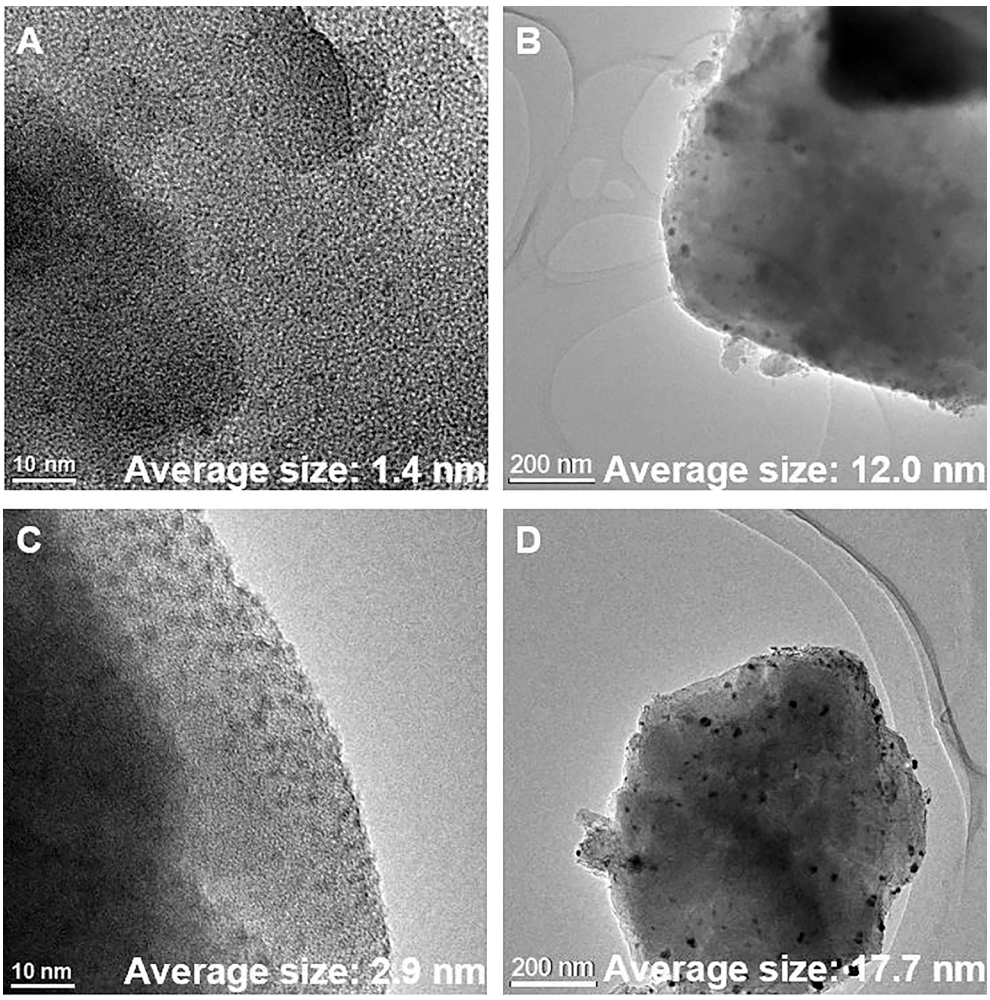

Fig. 4. TEM images of the PNA samples before and after PNA test. A: Fredry. B: Fredry-used. C: 80dry. D: 80dry-used. Detailed statistics of average particle size are shown in Figure S4.

are the same at 220 °C and 330 °C, which can be attributed to NO released from ion-exchanged Pd sites. However, the amount of released NO from 80dry is significantly lower than that from Fredry, indicating that 80dry is more vulnerable to CO degradation and more ion-exchanged sites agglomerated into PdO nanoparticles. Due to CO reducing the Pd^{2+} sites instead of NO, the NO_2 release peaks disappeared at 160 °C. The generated PdO nanoparticles catalyze NO oxidation to NO_2, causing the NO_2 generation peaks at 230 °C and 470 °C. It can be seen the NO oxidation is more obvious on 80dry because more PdO nanoparticles were generated. In the following cycles with CO, both Fredry and 80dry were gradually deactivated, resulting in the decreasing peaks in both the NO and NO_2 profiles (Fig. 3 and Figure S3). In cycle 5 of 80dry, the desorption peak at 220 °C and 330 °C could be neglected, while Fredry could still store a certain amount of NO and release it at those temperatures. Note that a sharp NO desorption peak appeared at ~ 160 °C in cycle 5 of 80dry, which is attributed to the NO release from large Pd nanoparticles. This sharp peak is more obvious in cycle 7 (the last cycle with CO) of 80dry in Figure S3. The absence of this sharp peak in cycle 7 of Fredry also demonstrates that only a small percentage of Pd sites in Fredry were converted to large Pd nanoparticles.

Cycle 8 was further conducted without CO to reveal the PNA performance after CO degradation, as shown in Fig. 3. There is still one NO consumption peak (generating NO_2) at low temperatures and two NO release peaks at higher temperatures for both Fredry and 80dry samples. The NO consumption peaks at 160 °C are at the same temperature compared to the initial cycles, indicating that the Pd^{2+} species were still reduced by NO at the same temperature. The two NO release peaks in cycle 8 of both PNA samples shifted to lower temperatures, compared to the peaks in cycle 2. Therefore, it can be deduced that the high concentration of CO suppressed the interaction between Pd sites and NO, resulting in a lower release temperature of NO. The NO oxidation peak at 470 °C still appeared in cycle 8, demonstrating the Pd nanoparticles remained in 80dry after CO degradation.

Table 5
Properties of Pd sites in PNA samples.

	Dispersion	Pd surface amount (10^{-5}mol/gcat)	Diameter in TEM (nm)
Fredry	42.2 %	3.98	1.4
Fredry used	15.7 %	1.48	12.0
80dry	29.1 %	2.74	2.9
80dry used	8.5 %	0.81	17.7

4.2. Sintering of Pd sites

To further investigate the influence of CO-induced degradation on PNA, we conducted several characterizations of the samples before and after the multicycle test. TEM was first conducted to determine the morphology of Pd/SSZ-13 samples, as shown in Fig. 4. More TEM images and the diameter statistics of Pd are shown in Figure S4. CO

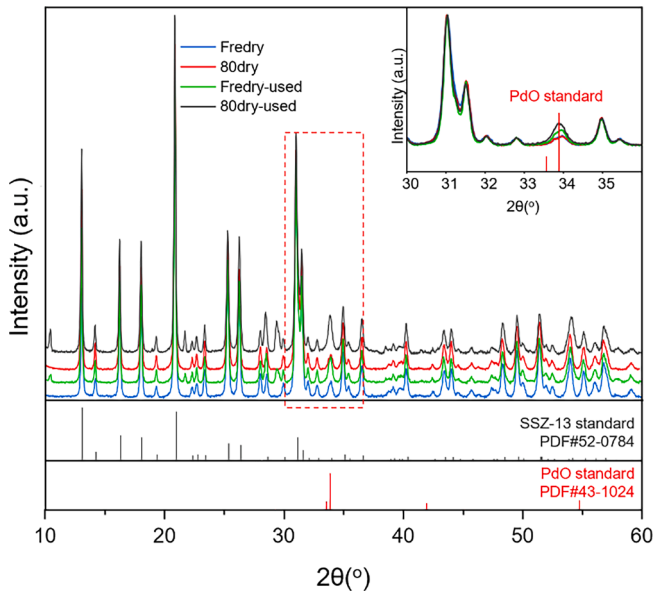

Fig. 5. XRD patterns of PNA samples before and after CO degradation.

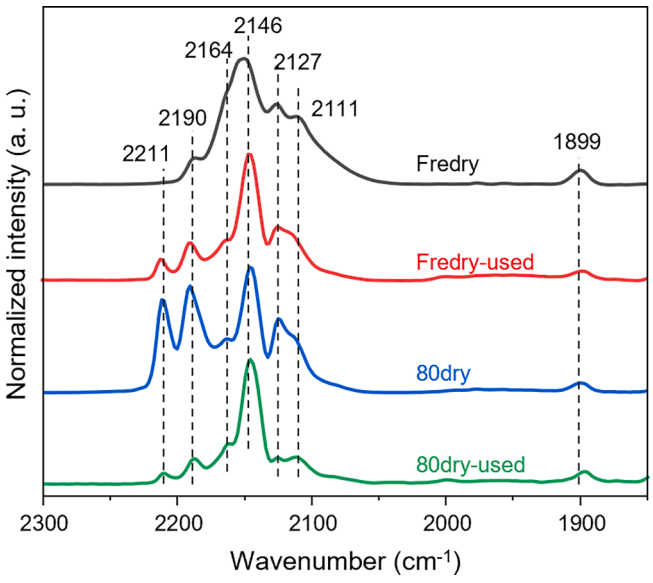

Fig. 6. In situ DRIFT of CO adsorption on PNA samples. The Pd/SSZ-13 sample first adsorbed 4000 ppm CO/Ar for 20 min at 30 °C, then it was purged by pure Ar for 5 min before collecting the spectra.

chemisorption was also conducted to determine the dispersion and the surface amount of Pd sites in all Pd/SSZ-13 samples, as shown in Table 5. Before the PNA evaluation, the Pd clusters are well-dispersed on the SSZ-13 supports in both Fredry and 80dry samples, with average diameters of 1.4 nm and 2.9 nm, respectively (Fig. 4). After the PNA test, the average sizes of Pd NPs increased to 12.0 nm (Fredry-used) and 17.7 nm (80dry-used), demonstrating that Pd sintering occurred in both samples during CO degradation. Fredry-used had a smaller Pd nanoparticle size than 80dry-used, showing a better resistance towards high CO concentration. It is also apparent that the dispersion of Pd decreased to 15.7 % (Fredry-used) and 8.5 % (80dry-used) (Table 5), demonstrating that the Fredry sample suffered a 63 % loss and 80dry a 71 % loss of exposed Pd surface species. Therefore, we could deduce that the freeze-drying process can suppress the mobility of Pd species because the $Pd(NO_3)_2$ solution tends to stay inside SSZ-13 channel and sublimate. At 80 °C drying, the $Pd(NO_3)_2$ solution likely preferably moves outside the SSZ-13 channels forming PdO_x clusters. The Pd sites inside SSZ-13 channels are more stable towards high CO concentration, resulting in less surface Pd site loss in the Fredry sample and a better stability. Notably, the particle size distributions of Fredry-used and 80dry-used samples are relatively more non-uniform compared to the fresh samples (Figure S4). This is because the formed large Pd nanoparticle have better stability to anchor small Pd species, leading to an uneven sintering rate of Pd clusters with different diameters [19,20].

To further confirm the agglomeration of Pd sites on different Pd/SSZ-13 samples, XRD was conducted for all the Pd/SSZ-13 samples to determine the status of both Pd sites and the SSZ-13 support, as shown in Fig. 5. Both Fredry and 80dry samples evidently contain well-crystalized SSZ-13. Furthermore, the diffraction peaks of SSZ-13 can also be identified from the XRD patterns after the PNA test, indicating the CO degradation did not have a considerable influence on the SSZ-13 supports. The diffraction peak at $2\theta = 33.8°$ is the characteristic peak of the PdO(1 0 1) phase. To better distinguish the peaks in the different samples the XRD patterns are sorted and enlarged in this region, as shown in the upper right corner of Fig. 5. The PdO(1 0 1) diffraction peaks at $2\theta = 33.8°$ of Fredry and 80dry before the test completely overlap and present a board shape, indicating that the Pd sites are well dispersed. After the PNA test, both the PdO(1 0 1) diffraction peaks of Fredry-used and 80dry-used increased, where the peak for 80dry-used is more intense than the one for Fredry because of the larger PdO nanoparticles. These results are all consistent with the TEM and CO chemisorption results, indicating that the Pd sites sintered after CO degradation, and Fredry is more resistant than 80dry towards the CO-induced Pd agglomeration.

From the TEM, CO chemisorption and XRD results, it is clearly shown that the Pd sites on both Fredry and 80dry samples are agglomerated to Pd nanoparticles or larger Pd nanoparticles under the high CO concentration, which is the main reason for PNA degradation. Meanwhile, the Pd sites of the Fredry sample showed a better stability towards the CO-induced sintering. To further discriminate the changes in different Pd sites in Fredry and 80dry, in-situ DRIFT during CO adsorption was subsequently conducted as shown in Fig. 6. CO has been widely used as a probe molecule to detect the different Pd sites on zeolites [41–48]. The Pd/SSZ-13 sample first adsorbed 4000 ppm CO/Ar for 20 min at 30 °C, then it was purged by pure Ar for 5 min to remove the weakly adsorbed and gas phase CO. The peaks 2211 cm^{-1} and 2190 cm^{-1} can be attributed to CO adsorbed on Pd^{+2}/2Al ions [44,47]. Compared to the Fredry sample, there are more Pd^{2+}/2Al ions existing on the 80dry sample, while they are vulnerable towards CO degradation because the CO-Pd^{2+}/2Al peak intensity decreases for the 80dry-used sample. The peak at 2111 cm^{-1} can be attributed to linearly adsorbed CO on metallic Pd clusters [49,50], and the one at 1895 cm^{-1} assigned to bridged carbonyls on Pd^0 and multi-bridged carbonyls on small Pd clusters [43,48]. After CO degradation, the relative intensity of linear CO-Pd^0 decreased for both samples, indicating the agglomeration of Pd^0 sites happens under high CO concentration. The peaks at 2127 cm^{-1} and 2146 cm^{-1} represent CO adsorption on ionic $ZPd(OH)^+$ complexes [43,46,47], and the peak at 2164 cm^{-1} can be attributed to CO adsorption on surface $[Pd(OH)]^+$ [50–52]. The CO-$ZPd(OH)^+$ peaks are dominant among all the peaks before and after CO degradation over both Fredry and 80dry samples, indicating the $ZPd(OH)^+$ sites have a better stability towards CO degradation than other Pd sites. It is clearly demonstrated from the spectra that the Fredry sample contains more stable $ZPd(OH)^+$ sites, while the proportion of PdO_x clusters and Pd^{2+}/2Al in the 80dry sample is higher. This is because during the freeze-drying procedure, the impregnated Pd ionic solution was frozen inside the SSZ-13 channel and this was more favorable to form ion-exchanged Pd sites after drying. In contrast, during the drying process at 80 °C, the Pd ionic solution more favorably migrates outside SSZ-13 channels to form PdO_x clusters. Furthermore, it also can be inferred from the change of relative intensity of CO-Pd^0 peaks that the stability of Pd^0 clusters on Fredry is higher than that for 80dry. This is because the freeze-drying process assists the generation of Pd^0/PdO clusters inside the SSZ-13 channel, which can

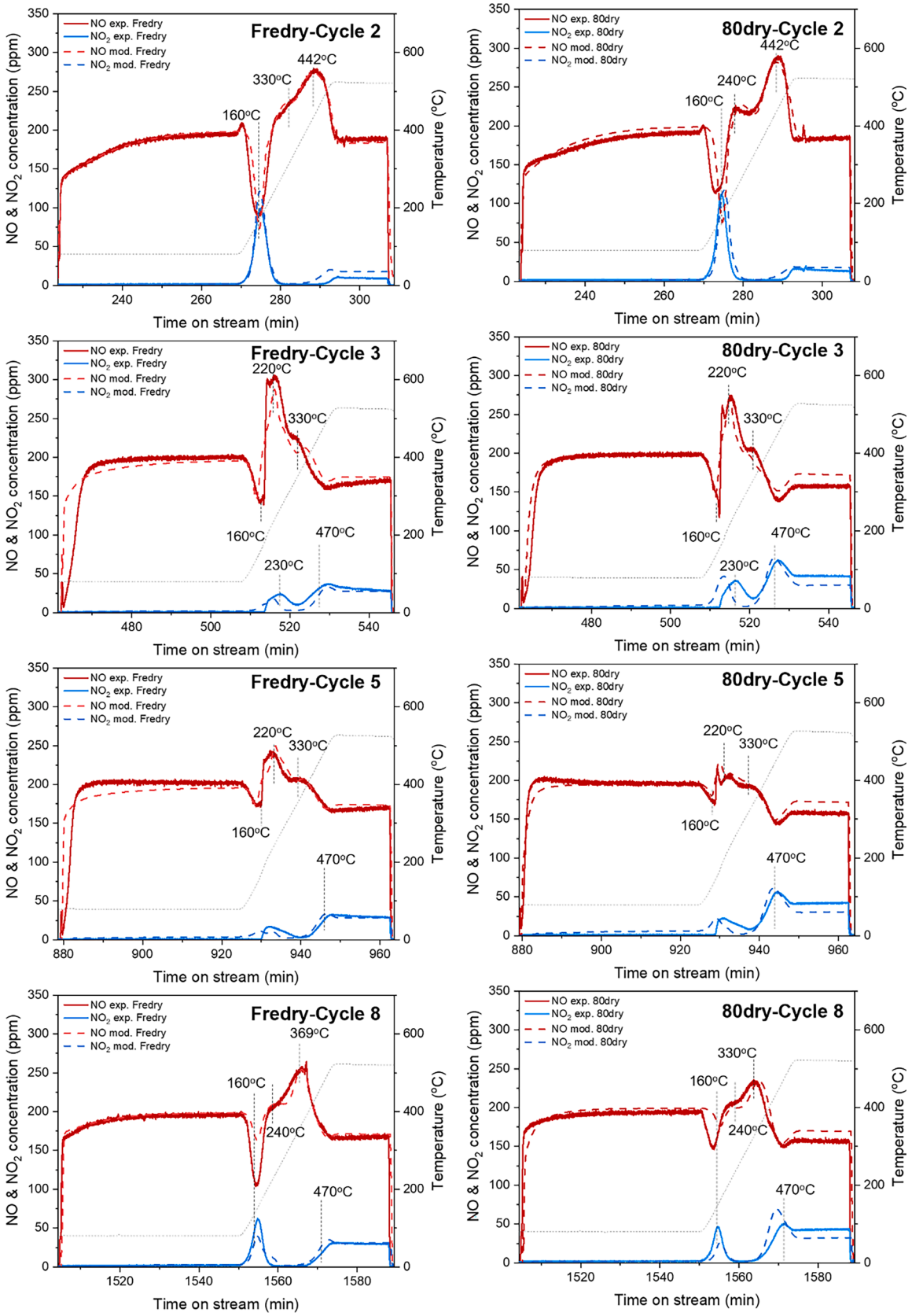

Fig. 7. NO and NO_2 profiles of selected PNA cycles in experimental evaluation and kinetic modeling over Fredry and 80dry samples. Reaction conditions: 200 ppm NO_x, 4000 ppm CO (in cycle 3-cycle 7), 5 %H_2O, 8 % O_2. Full-cycle profiles are shown in Figure S5–S7.

Table 6
Attributed reactions for peaks according to kinetic model results.

Cycles	Peak temperature (°C)	Corresponding reactions
1–2	160	$Z^-Pd^{2+}Z^-$–NO_2 desorption (R2) $Z^-[PdOH]^+$ reduction (R4) and Z^-Pd^- adsorb NO (R5) $Pd(NO_3)_2$ formation and decomposition (R7, R8)
	240	$Z^-Pd^{2+}Z^-$–NO desorption in 80dry (R1)
	330	$Z^-Pd^{2+}Z^-$–NO desorption in Fredry (R1)
	442	Z^-Pd^-–NO desorption (R5)
3–7	160	Pd^e and Pd^N adsorb NO (R27, R33) Pd^N-NO desorption (R33)
	220	Pd^e-NO desorption (R27)
	230	Pd^e-NO oxidation (R28)
	330	Z^-H^+-Pd^0-NO desorption (R13, R21)
	470	NO oxidation on Pd/PdO (R30, R36)
8	160	$Z^-[PdOH]^+$ reduction (R4) and Z^-Pd^- adsorb NO (R5)
	240	$Z^-Pd^{2+}Z^-$–NO desorption (R1)
	330	Z^-Pd^-–NO desorption in 80dry (R5)
	369	Z^-Pd^-–NO desorption in Fredry (R5)
	470	NO oxidation on Pd/PdO (R30, R36)

specially restrict agglomeration. After the PNA test under a high CO concentration, a great loss of CO-Pd^0 peak intensity could be seen for the 80dry sample, indicating that the PdO_x clusters are more vulnerable to a high CO concentration causing their migration into large Pd nanoparticles with less exposed surface Pd sites. Note that the peak at 2146 cm^{-1} still dominates for both the Fredry-used and 80dry-used samples, demonstrating that there is still a considerable amount of $ZPd(OH)^+$ that existing after CO degradation.

4.3. Kinetic model for CO induced degradation

Owing to the different changes in PdO_x sites and ion-exchanged Pd sites after CO degradation, it is important to investigate the different sintering modes of these Pd sites, and obtain knowledge for increasing the stability of Pd sites when designing PNA materials. Herein, we conducted kinetic modeling for the PNA performance of both Fredry and 80dry. The kinetic model used is from our previously reported work [17], which contains (1) NO_x adsorption on initial Pd sites, (2) Pd^{2+} sites reduced by CO, (3) Ostwald ripening of initial Pd sites to Pd nanoparticles, and (4) Pd particle migration to form large Pd nanoparticles. Detailed information about this kinetic model and reaction steps can be found above in Section 3. *Kinetic modeling*.

All the parameters for the kinetic modeling are listed in Table S2 and Table S3. As demonstrated via in situ DRIFT of CO adsorption (Fig. 6), there is a considerable amount of ion-exchanged Pd sites still existing after CO degradation, while most of the PdO_x sites sintered. Furthermore, it can be seen in Fig. 1 that the NO_x desorption peaks before adding CO (Cycle 2) and after adding CO (Cycle 8) were in different positions. These results indicate that the high CO concentration also weakened the interaction between NO_x and ion-exchanged Pd sites, resulting in the desorption peak shifting to a lower temperature after CO degradation. Therefore, different parameter values were used for the ion-exchanged Pd sites before and after cycle 3 for the simulation. The experimental and kinetic modeling results of selected cycles are shown in Fig. 7, and the full-cycle results are shown in Figure S5 to Figure S7.

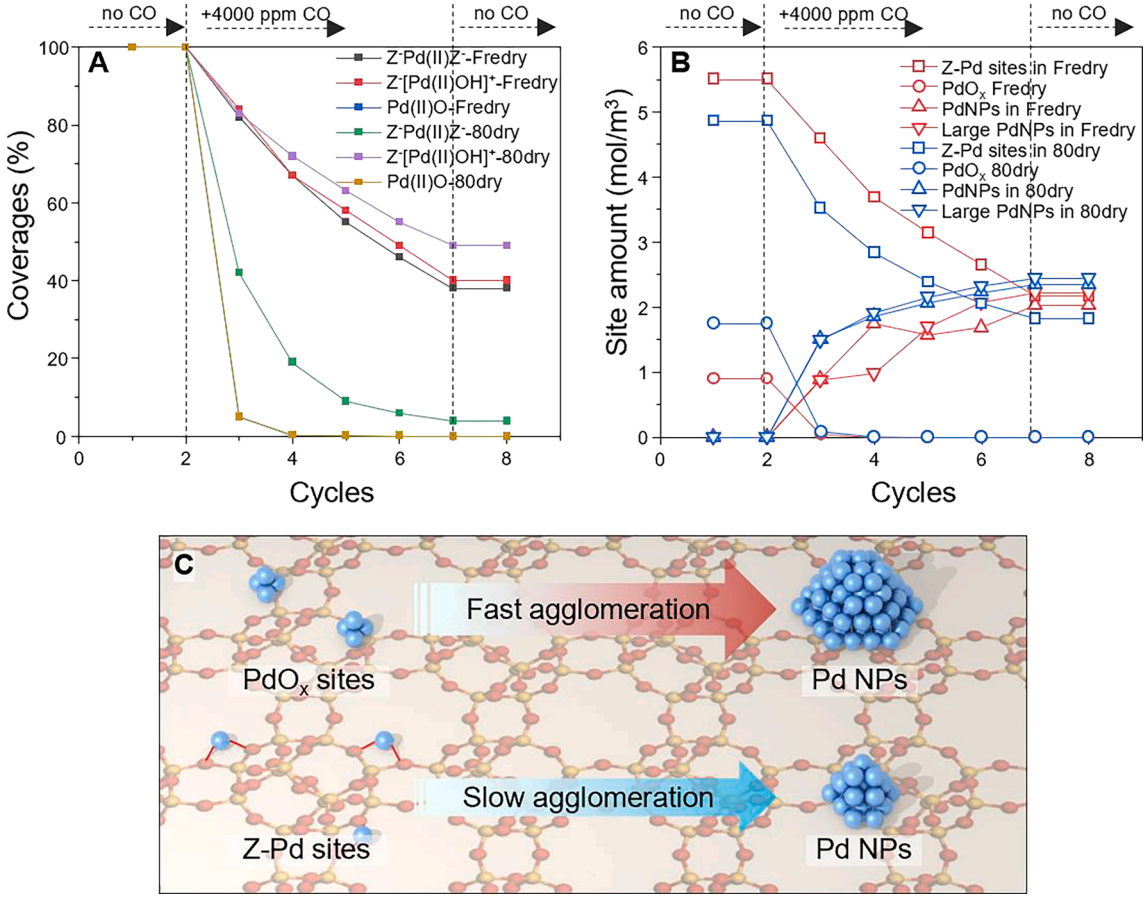

Fig. 8. Model-predicted coverage of initial Pd sites (A) and amount of Pd sites (B) of Fredry and 80dry samples in each cycle. C: Mechanism of sintering of different Pd sites.

The NO_x profiles from experiments and kinetic simulations agree well for both Fredry and 80dry samples, indicating that the CO degradation behaviors of Fredry and 80dry still follow our kinetic model with NO_x storage, Ostwald ripening and particle migration [17]. Owing to a large quantity of Pd sites and adsorbed species changing during the PNA evaluation process, the coverage data for all species obtained from the kinetic simulation is massive. Herein, we only summarize the peaks attributed in each cycle to the species coverage of the kinetic model, as listed in Table 6. All the peaks are also marked in Fig. 7 to enable a better understanding.

From the kinetic model results (Fig. 7 and Table 5) in cycle 2, it can be seen that both $Z^-Pd^{2+}Z^-$ and $Z^-[PdOH]^+$ adsorb NO_x species at the beginning of the cycle. The first NO consumption peak and NO_2 generation peak appear at 160 °C, which can be attributed to $Z^-Pd^{2+}Z^-$–NO_2 desorption (R2), $Z^-[PdOH]^+$ reduction to Z^-Pd^- (R4) and subsequently adsorbed NO (R5). $Pd(NO_3)_2$ formation and decomposition (R7, R8) also contribute to these peaks. The temperatures of NO desorbed from $Z^-Pd^{2+}Z^-$ were different for Fredry (330 °C) and 80dry (240 °C). This is because the different drying processes influenced the properties of the ion-exchanged Pd sites. The peak at 442 °C can be attributed to NO release from Z^-Pd^- because it has strong interaction with NO [23,40,53].

From cycle 3, 4000 ppm CO was added to simulate a high-concentration CO pulse. Most of the initial Pd species, i. e., $Z^-Pd^{2+}Z^-$, $Z^-[PdOH]^+$ and PdO, did not contribute to NO_x adsorption and release. Instead, they were reduced to metallic sites, Z^-H^+-Pd^0 and Pd^0 (R13, R15, R19). All the metallic Pd sites started to agglomerate to Pd NPs via the Ostwald ripening process (described in Table 3), and the Pd NPs sites migrated to large Pd NPs at a lower sintering rate (described in Table 4). Therefore, the peak positions are changed in cycle 3. The new peaks at 160 °C, 220 °C, 230 °C, and 470 °C are attributed to NO_x desorption and NO oxidation on Pd NPs (R27-R30), while the peak at 330 °C can be attributed to the NO release from Z^-H^+-Pd^0 sites that have not sintered. Note that there is an extra NO release peak at ~ 160 °C in cycle 3 of 80dry, which is more obvious in cycle 5 and cycle 7 (Figure S7). This peak is attributed to the NO release from large Pd NPs, indicating that a greater quantity of large Pd NPs is generated in 80dry than in Fredry during CO degradation. Comparing the NO and NO_2 profiles from cycle 3 to cycle 7 (Figure S7), the peak positions did not change but the amount of adsorbed NO_x decreased. This result indicates that there are no new Pd sites generated but instead the Pd sites were gradually sintered.

Cycle 8 was conducted in the absence of CO. According to our in-situ DRIFT spectra (Fig. 6), part of the initial ion-exchanged Pd sites remained after CO degradation. Therefore, the peaks attributed to $Z^-[PdOH]^+$ reduction (160 °C, R4), $Z^-Pd^{2+}Z^-$–NO desorption (240 °C, R1), and Z^-Pd^-–NO desorption (330 °C for 80dry and 369 °C for Fredry, R5) still appeared. Notably, the NO release peaks from ion-exchanged sites shifted to a lower temperature compared to the profiles before CO degradation, indicating that the high CO concentration also changed the binding strength between Pd sites and NO_x species. The peak at 470 °C remained in cycle 8, originating from NO oxidation on Pd/PdO nanoparticles. This peak for 80dry is much more significant than that for Fredry, suggesting that more Pd NPs were generated on the 80dry sample, which is consistent with our characterization results regarding Pd agglomeration.

4.4. Sintering mechanism of different Pd sites

The coverages of the initial Pd sites combined with the formed surface species during NO and NO_2 adsorption were simulated using the kinetic model to investigate the degradation behavior of the different Pd sites. The Pd sites in their reversibly reduced or reacted forms are considered as the same sites because they share the same coverage. Thus the coverages of $Z^-Pd^{2+}Z^-$, $Z^-[PdOH]^+/Z^-Pd^-$, $PdO/Pd(NO_3)_2$ were separately summarized, as shown in Fig. 8A. Apparently, PdO sites in both Fredry and 80dry drastically deactivated in the first cycle (cycle 3) with 4000 ppm CO (note that the yellow and blue lines are overlapping), while $Z^-Pd^{2+}Z^-$ and $Z^-[PdOH]^+$ gradually deactivated over all cycles 3–7. The $Z^-Pd^{2+}Z^-$ on 80dry lost its coverage faster than Fredry, showing that the ion-exchanged Pd sites on Fredry are more resistant towards CO degradation. This result is consistent with our PNA performance results and characterizations. Fig. 8B shows the amount of ion-exchanged Pd sites (Z-Pd), initial PdO_x clusters, Pd NPs and large Pd NPs in each cycle. It is clear that the ion-exchanged Pd site has greater tolerance towards the high CO concentration than the PdO_x sites. Meanwhile, it is evident that the agglomeration of Pd NPs to large Pd NPs on the Fredry sample is only slightly slower than the same process on 80dry, but this difference in rates is negligible. According to the coverages and amount of Pd sites, the degradation mode of the different Pd sites can be deduced as shown in Fig. 8C. Compared to the ion exchanged Pd sites, PdO_x sites are more vulnerable to CO degradation, and further, more vulnerable to CO-induced Ostwald ripening. With the presence of CO, both ion-exchanged Pd sites and PdO sites formed Pd carbonyls, which have a high mobility at room temperature [18]. The Pd carbonyls formed from ion-exchanged Pd sites are restricted by the SSZ-13 channel, which further suppresses the Ostwald ripening. After forming Pd nanoparticles, Ostwald ripening contributes less to deactivation owing to the relatively higher stability of surface Pd atoms on large-size PdO NPs [19]. Particle migration of PdO NPs becomes dominant and contributes almost equally to the degradation of both Fredry and 80dry samples.

5. Conclusions

In this work, we fabricated a novel form of Pd/SSZ-13 by using a freeze-drying process after incipient wetness impregnation. A multicycle PNA evaluation with high CO concentration was conducted to simulate the multicycle cold start periods of an engine. Under extremely concentrated CO (~4000 ppm), the freeze-dried Pd/SSZ-13 was found to have better stability than the sample prepared by the more common process of drying at 80 °C. Especially, the freeze-dried Pd/SSZ-13 maintained the same NO_x storage amount after the first cycle of CO degradation, while in the same cycle, the 80 °C-dried Pd/SSZ-13 suffered from a huge loss of NO_x storage amount. Several characterization techniques, including XRD, CO chemisorption and TEM were conducted on the Pd/SSZ-13 before and after the PNA test, and it was clearly found that the Pd sites on the freeze-dried sample were more stable towards CO-induced agglomeration. Combing in-situ DRIFT and a kinetic modelling study, we found that the freeze-dried Pd/SSZ-13 had more ion-exchanged Pd sites than 80 °C-dried Pd/SSZ-13. The ion-exchanged Pd sites in SSZ-13 have greater resistance towards the CO-induced Ostwald ripening process, consequently suppressing the sintering behavior under a high concentration of CO. These findings provide potential ideas to design PNA materials with increased stability under conditions with extremely high CO concentration pulses from incomplete fuel combustion during cold start.

Declaration of Competing Interest

The authors declare that they have no known competing financial interests or personal relationships that could have appeared to influence the work reported in this paper.

Data availability

Data will be made available on request.

Acknowledgment

This work was achieved at the Division of Chemical Engineering and the Competence Center for Catalysis, Chalmers University of Technology in Gothenburg, Sweden, in collaboration with AVL List GmbH in Graz, Austria. This project is funded from the European Union's Horizon 2020

research and innovation programme under grant agreement no 874972.

Appendix A. Supplementary data

Supplementary data to this article can be found online at https://doi.org/10.1016/j.cej.2023.141681.

References

[1] A. Wang, K. Lindgren, M. Di, D. Bernin, P.-A. Carlsson, M. Thuvander, L. Olsson, Insight into hydrothermal aging effect on Pd sites over Pd/LTA and Pd/SSZ-13 as PNA and CO oxidation monolith catalysts, Appl. Catal. B-Environ. 278 (2020), 119315, https://doi.org/10.1016/j.apcatb.2020.119315.

[2] J. Lee, J.R. Theis, E.A. Kyriakidou, Vehicle emissions trapping materials: Successes, challenges, and the path forward, Appl. Catal. B-Environ. 243 (2019) 397–414, https://doi.org/10.1016/j.apcatb.2018.10.069.

[3] A. Wang, L. Olsson, The impact of automotive catalysis on the United Nations sustainable development goals, Nat. Catal. 2 (7) (2019) 566–570, https://doi.org/10.1038/s41929-019-0318-3.

[4] C. Weber, I. Sundvor, E. Figenbaum, Comparison of regulated emission factors of Euro 6 LDV in Nordic temperatures and cold start conditions: Diesel- and gasoline direct-injection, Atmos. Enviro. 206 (2019) 208–217, https://doi.org/10.1016/j.atmosenv.2019.02.031.

[5] R.F. Ilmasani, D. Yao, P.H. Ho, D. Bernin, D. Creaser, L. Olsson, Deactivation of phosphorus-poisoned Pd/SSZ-13 for the passive adsorption of NOx, J. Environ. Chem. Eng. 10 (3) (2022), 107608, https://doi.org/10.1016/j.jece.2022.107608.

[6] Y. Gu, W.S. Epling, Passive NOx adsorber: An overview of catalyst performance and reaction chemistry, Appl. Catal. A-Gen. 570 (2019) 1–14, https://doi.org/10.1016/j.apcata.2018.10.036.

[7] R.F. Ilmasani, J. Woo, D. Creaser, L. Olsson, Influencing the NOx stability by metal oxide addition to Pd/BEA for passive NOx adsorbers, Ind. Eng. Chem. Res. 59 (21) (2020) 9830–9840, https://doi.org/10.1021/acs.iecr.9b06976.

[8] P. Kunal, T.J. Toops, M.K. Kidder, M.J. Lance, Deactivation trends of Pd/SSZ-13 under the simultaneous presence of NO, CO, hydrocarbons and water for passive NOx adsorption, Appl. Catal. B-Environ. 299 (2021), 120591, https://doi.org/10.1016/j.apcatb.2021.120591.

[9] M. Ambast, A. Gupta, B.M.M. Rahman, L.C. Grabow, M.P. Harold, NOx adsorption with CO and C_2H_4 on Pd/SSZ-13: Experiments and modeling, Appl. Catal. B-Environ. 286 (2021), 119871, https://doi.org/10.1016/j.apcatb.2020.119871.

[10] J. Gao, G. Tian, A. Sorniotti, A.E. Karci, R. Di Palo, Review of thermal management of catalytic converters to decrease engine emissions during cold start and warm up, Appl. Therm. Eng. 147 (2019) 177–187, https://doi.org/10.1016/j.applthermaleng.2018.10.037.

[11] P.H. Ho, D. Yao, D. Creaser, L. Olsson, Advantages of High-Siliceous Zeolites in the Reactivity and Stability of Diesel Oxidation Catalysts, ACS Eng. Au (2022), https://doi.org/10.1021/acsengineeringau.1c00035.

[12] Y. Gu, R.P. Zelinsky, Y.-R. Chen, W.S. Epling, Investigation of an irreversible NOx storage degradation Mode on a Pd/BEA passive NOx adsorber, Appl. Catal. B-Environ. 258 (2019), 118032, https://doi.org/10.1016/j.apcatb.2019.118032.

[13] Y. Gu, S. Marino, M. Cortés-Reyes, I.S. Pieta, J.A. Pihl, W.S. Epling, Integration of an Oxidation Catalyst with Pd/Zeolite-Based Passive NOx Adsorbers: Impacts on Degradation Resistance and Desorption Characteristics, Ind. Eng. Chem. Res. 60 (18) (2020) 6455–6464, https://doi.org/10.1021/acs.iecr.0c05186.

[14] J.R. Theis, J.A. Ura, Assessment of zeolite-based Low temperature NOx adsorbers: Effect of reductants during multiple sequential cold starts, Catal. Today 360 (2021) 340–349, https://doi.org/10.1016/j.cattod.2020.01.040.

[15] Y. Ryou, J. Lee, Y. Kim, S. Hwang, H. Lee, C.H. Kim, D.H. Kim, Effect of reduction treatments (H_2 vs. CO) on the NO adsorption ability and the physicochemical properties of Pd/SSZ-13 passive NOx adsorber for cold start application, Appl. Catal. A-Gen. 569 (2019) 28–34, https://doi.org/10.1016/j.apcata.2018.10.016.

[16] E. Bello, V.J. Margarit, E.M. Gallego, F. Schuetze, C. Hengst, A. Corma, M. Moliner, Deactivation and regeneration studies on Pd-containing medium pore zeolites as passive NOx adsorbers (PNAs) in cold-start applications, Micro. Meso. Mater. 302 (2020), 110222, https://doi.org/10.1016/j.micromeso.2020.110222.

[17] D. Yao, R.F. Ilmasani, J.C. Wurzenberger, T. Glatz, J. Han, P.H. Ho, D. Creaser, L. Olsson, Insight into CO induced degradation mode of Pd/SSZ-13 in NOx adsorption and release: Experiment and modeling, Chem. Eng. J. 439 (2022), 135714, https://doi.org/10.1016/j.cej.2022.135714.

[18] G.S. Parkinson, Z. Novotny, G. Argentero, M. Schmid, J. Pavelec, R. Kosak, P. Blaha, U. Diebold, Carbon monoxide-induced adatom sintering in a Pd-Fe3O4 model catalyst, Nat. Mater. 12 (8) (2013) 724–728, https://doi.org/10.1038/nmat3667.

[19] T.W. Hansen, A.T. DeLaRiva, S.R. Challa, A.K. Datye, Sintering of Catalytic Nanoparticles: Particle Migration or Ostwald Ripening? Acc. Chem. Res. 46 (8) (2013) 1720–1730, https://doi.org/10.1021/ar3002427.

[20] S.R. Challa, A.T. Delariva, T.W. Hansen, S. Helveg, J. Sehested, P.L. Hansen, F. Garzon, A.K. Datye, Relating Rates of Catalyst Sintering to the Disappearance of Individual Nanoparticles during Ostwald Ripening, J. Am. Chem. Soc. 133 (51) (2011) 20672–20675, https://doi.org/10.1021/ja208324n.

[21] Q. Xu, K.C. Kharas, B.J. Croley, A.K. Datye, The Sintering of Supported Pd Automotive Catalysts, ChemCatChem 3 (6) (2011) 1004–1014, https://doi.org/10.1002/cctc.201000392.

[22] A. Wang, K. Xie, A. Kumar, K. Kamasamudram, L. Olsson, Layered Pd/SSZ-13 with Cu/SSZ-13 as PNA – SCR dual-layer monolith catalyst for NOx abatement, Catal. Today (2020) 356–366, https://doi.org/10.1016/j.cattod.2020.01.035.

[23] D. Yao, R.F. Ilmasani, J.C. Wurzenberger, T. Glatz, J. Han, A. Wang, D. Creaser, L. Olsson, Kinetic modeling of CO assisted passive NOx adsorption on Pd/SSZ-13, Chem. Eng. J. 428 (2022), 132459, https://doi.org/10.1016/j.cej.2021.132459.

[24] Z. Chen, M. Wang, J. Wang, C. Wang, J. Wang, W. Li, M. Shen, Investigation of crystal size effect on the NOx storage performance of Pd/SSZ-13 passive NOx adsorbers, Appl. Catal. B-Environ. 291 (2021), https://doi.org/10.1016/j.apcatb.2021.120026.

[25] Y. Ryou, J. Lee, S.J. Cho, H. Lee, C.H. Kim, D.H. Kim, Activation of Pd/SSZ-13 catalyst by hydrothermal aging treatment in passive NO adsorption performance at low temperature for cold start application, Appl. Catal. B-Environ. 212 (2017) 140–149, https://doi.org/10.1016/j.apcatb.2017.04.077.

[26] K. Wijayanti, S. Andonova, A. Kumar, J. Li, K. Kamasamudram, N.W. Currier, A. Yezerets, L. Olsson, Impact of sulfur oxide on NH3-SCR over Cu-SAPO-34, Appl. Catal. B-Environ. 166 (2015) 568–579, https://doi.org/10.1016/j.apcatb.2014.11.043.

[27] L. Olsson, H. Sjövall, R.J. Blint, A kinetic model for ammonia selective catalytic reduction over Cu-ZSM-5, Appl. Catal. B-Environ. 81 (3–4) (2008) 203–217, https://doi.org/10.1016/j.apcatb.2007.12.011.

[28] L. Olsson, K. Wijayanti, K. Leistner, A. Kumar, S.Y. Joshi, K. Kamasamudram, N. W. Currier, A. Yezerets, A multi-site kinetic model for NH3-SCR over Cu/SSZ-13, Appl. Catal. B-Environ. 174 (2015) 212–224, https://doi.org/10.1016/j.apcatb.2015.02.037.

[29] L. Olsson, K. Wijayanti, K. Leistner, A. Kumar, S.Y. Joshi, K. Kamasamudram, N. W. Currier, A. Yezerets, A kinetic model for sulfur poisoning and regeneration of Cu/SSZ-13 used for NH_3-SCR, Appl. Catal. B-Environ. 183 (2016) 394–406, https://doi.org/10.1016/j.apcatb.2015.11.001.

[30] Supriyanto, K. Wijayanti, A. Kumar, S. Joshi, K. Kamasamudram, N.W. Currier, A. Yezerets, L. Olsson, Olsson, Global kinetic modeling of hydrothermal aging of NH3-SCR over Cu-zeolites, Appl. Catal. B-Environ. 163 (2015) 382–392.

[31] O. Mihai, L. Trandafilović, T. Wentworth, F.F. Torres, L. Olsson, The Effect of Si/Al Ratio for Pd/BEA and Pd/SSZ-13 Used as Passive NOx Adsorbers, Top. Catal. 61 (18–19) (2018) 2007–2020, https://doi.org/10.1007/s11244-018-1017-z.

[32] S. Yasumura, H. Ide, T. Ueda, Y. Jing, C. Liu, K. Kon, T. Toyao, Z. Maeno, K.-I. Shimizu, Transformation of Bulk Pd to Pd Cations in Small-Pore CHA Zeolites Facilitated by NO, JACS Au 1 (2) (2021) 201–211, https://doi.org/10.1021/jacsau.0c00112.

[33] A.L. GmbH, AVL BOOST Aftertreatment Manual, (2020).

[34] D. Chatterjee, T. Burkhardt, B. Bandl-Konrad, T. Braun, E. Tronconi, I. Nova, C. Ciardelli, Numerical simulation of ammonia SCR-catalytic converters: Model development and application, SAE Trans. 114 (2005) 437–448. https://www.jstor.org/stable/44720971.

[35] S. Shwan, L. Olsson, M. Skoglundh, J. Jansson, Kinetic modeling of Fe-BEA as NH3-SCR catalyst—effect of phosphorous, AIChE J. 61 (1) (2015) 215–223, https://doi.org/10.1002/aic.14638.

[36] X. Auvray, W. Partridge, J.-S. Choi, J. Pihl, F. Coehlo, A. Yezerets, K. Kamasamudram, N. Currier, L. Olsson, Kinetic modeling of NH_3-SCR over a supported Cu zeolite catalyst using axial species distribution measurements, Appl. Catal. B-Environ. 163 (2015) 393–403, https://doi.org/10.1016/j.apcatb.2014.08.003.

[37] L. Olsson, M. Fredriksson, R.J. Blint, Kinetic modeling of sulfur poisoning and regeneration of lean NOx traps, Appl. Catal. B-Environ. 100 (1–2) (2010) 31–41, https://doi.org/10.1016/j.apcatb.2010.07.004.

[38] N. Wilken, K. Kamasamudram, N.W. Currier, J. Li, A. Yezerets, L. Olsson, Heat of adsorption for NH3, NO2 and NO on Cu-Beta zeolite using microcalorimeter for NH3 SCR applications, Catal. Today 151 (3) (2010) 237–243, https://doi.org/10.1016/j.cattod.2010.02.002.

[39] L. Olsson, H. Sjövall, R.J. Blint, Detailed kinetic modeling of NOx adsorption and NO oxidation over Cu-ZSM-5, Appl. Catal. B-Environ. 87 (3) (2009) 200–210, https://doi.org/10.1016/j.apcatb.2008.09.007.

[40] M. Ambast, K. Karinshak, B.M.M. Rahman, L.C. Grabow, M.P. Harold, Passive NOx adsorption on Pd/H-ZSM-5: Experiments and modeling, Appl. Catal. B-Environ. 269 (2020), 118802, https://doi.org/10.1016/j.apcatb.2020.118802.

[41] Y. Zheng, L. Kovarik, M.H. Engelhard, Y. Wang, Y. Wang, F. Gao, J. Szanyi, Low-temperature Pd/zeolite passive NOx adsorbers: structure, performance, and adsorption chemistry, J. Phys. Chem. C 121 (29) (2017) 15793–15803, https://doi.org/10.1021/acs.jpcc.7b04312.

[42] K. Honkala, P. Pirila, K. Laasonen, CO and NO adsorption and co-adsorption on the Pd(111) surface, Surf. Sci. 489 (2001), https://doi.org/10.1016/S0039-6028(01)01135-9.

[43] A.W. Aylor, L.J. Lobree, J.A. Reimer, A.T. Bell, Investigations of the Dispersion of Pd in H-ZSM-5, J. Catal. 172 (2) (1997) 453–462.

[44] K. Khivantsev, N.R. Jaegers, I.Z. Koleva, H.A. Aleksandrov, L. Kovarik, M. Engelhard, F. Gao, Y. Wang, G.N. Vayssilov, J. Szanyi, Stabilization of Super Electrophilic Pd+2 Cations in Small-Pore SSZ-13 Zeolite, J. Phys. Chem. C 124 (1) (2020) 309–321, https://doi.org/10.1021/acs.jpcc.9b06760.

[45] K. Chakarova, E. Ivanova, K. Hadjiivanov, D. Klissurski, H. Knözinger, Coordination chemistry of palladium cations in Pd-H-ZSM-5 as revealed by FTIR spectra of adsorbed and co-adsorbed probe molecules (CO and NO), Phys. Chem. Chem. Phys. 006 (13) (2004) 3702–3709, https://doi.org/10.1039/b401934b.

[46] K. Khivantsev, X. Wei, L. Kovarik, N.R. Jaegers, E.D. Walter, P. Tran, Y. Wang, J. Szanyi, Palladium/Ferrierite versus Palladium/SSZ-13 Passive NOx Adsorbers: Adsorbate-Controlled Location of Atomically Dispersed Palladium(II) in Ferrierite

Determines High Activity and Stability, Angew Chem Int Ed Engl 61 (3) (2022) e202107554.
[47] K. Khivantsev, N.R. Jaegers, L. Kovarik, J.C. Hanson, F.F. Tao, Y. Tang, X. Zhang, I. Z. Koleva, H.A. Aleksandrov, G.N. Vayssilov, Y. Wang, F. Gao, J. Szanyi, Achieving atomic dispersion of highly loaded transition metals in small-pore zeolite SSZ-13: High-capacity and high-efficiency low-temperature CO and passive NOx adsorbers, Angew. Chem. Int. Ed. 57 (51) (2018) 16672–16677, https://doi.org/10.1002/anie.201809343.
[48] L. Castoldi, R. Matarrese, S. Morandi, P. Ticali, L. Lietti, Low-temperature Pd/FER NOx adsorbers: Operando FT-IR spectroscopy and performance analysis, Catal. Today 360 (2021) 317–325, https://doi.org/10.1016/j.cattod.2020.02.019.
[49] H. Zhao, X. Chen, A. Bhat, Y. Li, J.W. Schwank, Insight into hydrothermal aging effect on deactivation of Pd/SSZ-13 as low-temperature NO adsorption catalyst: Effect of dealumination and Pd mobility, Appl. Catal. B-Environ. 286 (2021), https://doi.org/10.1016/j.apcatb.2020.119874.
[50] D. Chen, H. Lei, W. Xiong, Y. Li, X. Ji, J.-Y. Yang, B. Peng, M. Fu, P. Chen, D. Ye, Unravelling Phosphorus-Induced Deactivation of Pd-SSZ-13 for Passive NOx Adsorption and CO Oxidation, ACS Catal. (2021) 13891–13901, https://doi.org/10.1021/acscatal.1c03214.
[51] J. Luo, F. Gao, K. Kamasamudram, N. Currier, C.H.F. Peden, A. Yezerets, New insights into Cu/SSZ-13 SCR catalyst acidity. Part I: Nature of acidic sites probed by NH3 titration, J. Catal. 348 (2017) 291–299, https://doi.org/10.1016/j.jcat.2017.02.025.
[52] R. Villamaina, S. Liu, I. Nova, E. Tronconi, M.P. Ruggeri, J. Collier, A. York, D. Thompsett, Speciation of Cu Cations in Cu-CHA Catalysts for NH3-SCR: Effects of SiO2/AlO3 Ratio and Cu-Loading Investigated by Transient Response Methods, ACS Catal. 9 (10) (2019) 8916–8927, https://doi.org/10.1021/acscatal.9b02578.
[53] D. Mei, F. Gao, J. Szanyi, Y. Wang, Mechanistic insight into the passive NOx adsorption in the highly dispersed Pd/HBEA zeolite, Appl. Catal. A-Gen. 569 (2019) 181–189, https://doi.org/10.1016/j.apcata.2018.10.037.